Nuclear Instruments and Methods in Physics Research A ▮ (▮▮▮▮) ▮▮▮–▮▮▮

Contents lists available at ScienceDirect

Nuclear Instruments and Methods in Physics Research A

journal homepage: www.elsevier.com/locate/nima

Radiation tolerance of the CMS forward pixel detector

G.B. Cerati [a], M.E. Dinardo [b], A. Florez [c,1], S. Kwan [d], A. Lopez [c], S. Magni [a], S. Malvezzi [a], D. Menasce [a], L. Moroni [a,*], C.R. Newsom [e], D. Pedrini [a], M. Rovere [a], S. Sala [a], P. Tan [d], S. Taroni [a], M. Turqueti [d], L. Uplegger [d]

[a] Istituto Nazionale di Fisica Nucleare e Università Degli Studi Milano-Bicocca, Edificio U2, Piazza della Scienza 3, 20126 Milano, Italy
[b] University of Colorado at Boulder, Boulder, CO, USA
[c] University of Puerto Rico, Mayaguez, PR, USA
[d] Fermi National Accelerator Laboratory, Batavia, IL, USA
[e] University of Iowa, Iowa City, IA, USA

ARTICLE INFO

Article history:
Received 18 November 2008
Accepted 27 November 2008

Keywords:
Silicon pixel detector
Radiation tolerance

ABSTRACT

In this paper we present some results on the radiation tolerance of the CMS forward pixel detector. They were obtained from a beam test at Fermilab of a pixel-detector module, which was previously irradiated up to a maximum dose of 45 Mrad of protons at 200 MeV. It is shown that CMS forward pixel detector can tolerate this radiation dose without any major deterioration of its performance.

1. Introduction

The CMS forward pixel detector [1] is organized into four disks, two at each end of the barrel pixel detector. The design (Fig. 1) is in such a way to extend the tracking acceptance of the global pixel system up to a rapidity of $\eta=\pm 2.5$. The axial length of the three barrel elements is ~50 cm and their radii 4.4, 7.3 and 10.2 cm. The four disks are at ± 34.5 and ± 46.5 cm from the barrel center at the collision point and their inner and outer radii are 6.1 and 15.0 cm, respectively. The forward pixel modules (plaquettes) are arrays of different numbers of Read Out Chips (ROCs) bump-bonded to a single Si sensor of $n+/n$ type (see Fig. 2). The single pixel-cell dimensions are $150\,\mu m \times 100\,\mu m$.

The ROCs, designed by Horisberger's group at PSI, provide an analog readout of the collected charge and were produced with commercial 0.25 μm CMOS technology with radiation-tolerant design rules [2]. Each ROC serves a matrix of 52×80 sensor pixel cells and is bump-bonded to the sensor with the PbSn solder technology. The Si sensors, produced by SINTEF, employ a partially open p-stop isolation technology, are 270 μm thick and typically present a depletion voltage of around 50 V and a breakdown voltage well above 500 V. Details of the pixel sensors are shown in Fig. 3.

These detectors are expected to integrate a maximum dose of about 7 Mrad per year on the inner edge of the first disk at the full LHC design luminosity of $10^{34}\,cm^{-2}\,s^{-1}$ at 14 TeV center-of-mass energy. At higher radius, the integrated dose per year should decrease as $\sim r^{-1.8}$ [3]. To study the effects of such a high dose on the forward pixel detector performance, a pre-production plaquette of 2×4 ROCs was exposed to a peak dose of 45 Mrad at the Indiana University Cyclotron Facility using a 200 MeV proton beam. During the irradiation, the beam was centered on one edge of the plaquette to produce a highly non-uniform dose profile similar to that expected in the CMS forward pixels. The irradiation beam was roughly Gaussian in shape with $\sigma \sim 2$ cm. The geometry and characteristics of the irradiation are clearly illustrated in Fig. 4. Once completed the irradiation process, the plaquette was kept in a refrigerator at low temperature to avoid any annealing effect and was then tested on the test-beam at Fermilab.

2. Beam-test setup

To conduct the tests on the beam, a pixel telescope, which was previously developed for the BTeV project [4], was used. It consists of six pixel detector planes with $50 \times 400\,\mu m^2$ cells, allowing for an extrapolated track resolution of σ_x=4.9 μm, σ_y=6.2 μm on the plane normal to the beam at the position where the CMS pixels were placed and within an approximate transverse area of $0.5 \times 0.5\,cm^2$. The CMS pixel detectors under test were always orthogonal to the beam. An ad hoc data acquisition system, based on FPGAs [5], was developed to readout simultaneously the two types of devices and to build the events on the basis of a common time-stamp value. Synchronization was obtained by clocking the readout electronics with the accelerator RF, which was divided by two for instrumental reasons, 26.5 MHz=53 MHz/2.

*Corresponding author. Tel.: +39 0264482430; fax: +39 0264482463.
E-mail address: Luigi.Moroni@mib.infn.it (L. Moroni).
[1] Now at Vanderbilt University, Nashville, TN, USA.

0168-9002/$ - see front matter © 2008 Elsevier B.V. All rights reserved.
doi:10.1016/j.nima.2008.11.114

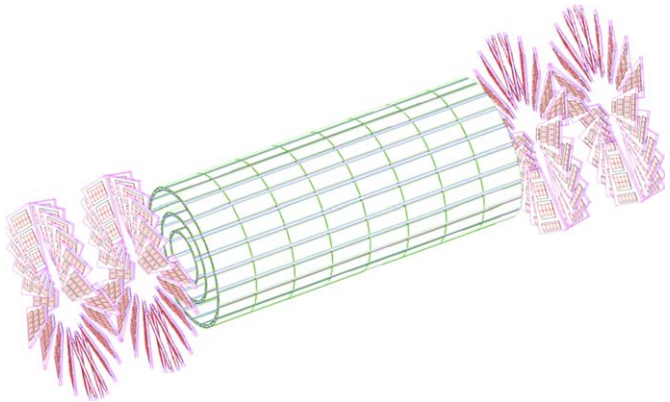

Fig. 1. A sketch of the CMS pixel detector with the three layers of the barrel detector and the four disks of the forward detector.

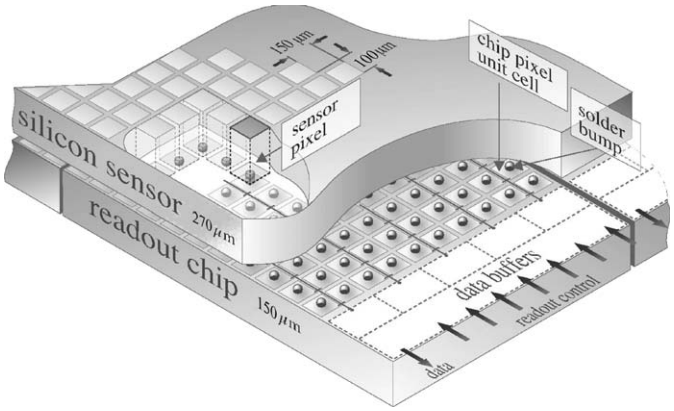

Fig. 2. A sketch of the hybrid structure of the forward pixel modules, plaquettes, resulting from bump-bonding several readout chips to a single pixelized Si sensor.

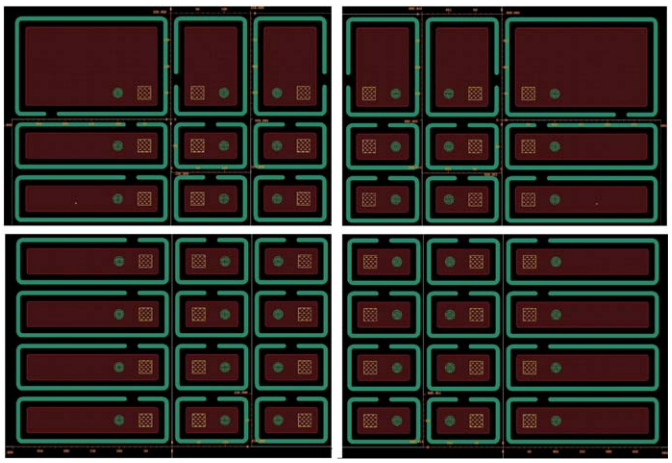

Fig. 3. The detailed design of a forward pixel sensor at the four corners of each ROC. In green are the p-stop rings around the pixel implants.

3. Results

For the sake of clarity we compare the results of the irradiated plaquette with those of a non-irradiated single ROC-plaquette, used as a reference. We will refer to the reference detector with ROC 0 and to the different regions of the plaquette with ROC 1…8, as labeled in Fig. 4.

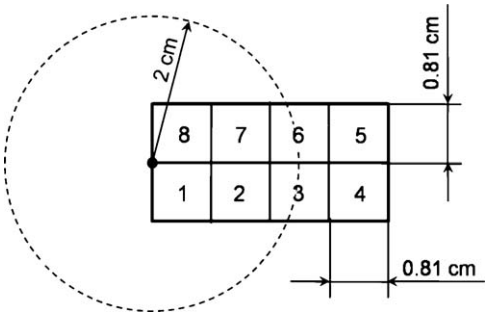

Fig. 4. The 2×4 irradiated plaquette. The numbers indicate the eight ROC's bump-bonded on the underlying sensor and the circle the position and the 1σ radius of the 200 MeV proton beam during the irradiation.

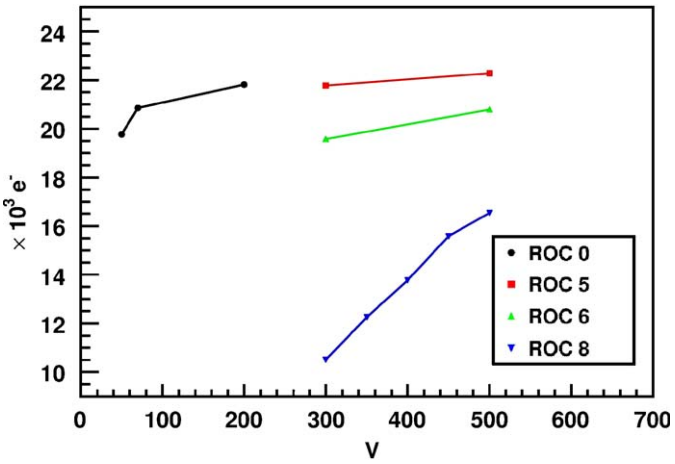

Fig. 5. MIP peak position at different bias voltages for the reference detector, ROC 0, and three regions of the irradiated detector, ROC 5, ROC 6 and ROC 8.

All the pixels were electronically calibrated using the internal calibration circuitry, which injects a known amount of charge into the pixel preamplifier input. The accuracy of the calibration is of the order of 8%. A common threshold was set for each ROC by choosing the lowest value at which the ROC was still practically immune from noise.[2] No fine tuning was done to equalize the thresholds on each channel: the resulting dispersion around the central value is about 10%. The final threshold setting was ~3800 e^- for the reference detector and ~3300 e^- for all the ROCs on the irradiated plaquette. The bias voltage was set at 200 V for the reference detector and at the maximum allowed by our power supply, 500 V, for the plaquette. As shown in Fig. 5, the first value is well above the depletion voltage, while the latter one is just below the depletion for the most irradiated region of the plaquette, corresponding to the ROC 8. In these conditions the detectors were tested on the M-test beam of the Fermilab Main Injector (120 GeV protons).

Fig. 6 shows the collected charge for the four ROCs we studied in details, namely ROC 0, ROC 5, ROC 6 and ROC 8.

The single-hit spectra,[3] on the first left column, show the charge collected by the sole pixel pointed by the telescope track when the impact point of the track is within the pixel-cell

[2] Unfortunately, our setup configuration was not optimal to allow for operation at low threshold.

[3] Fits to these spectra were obtained using the Landau distribution function available in the ROOT package [6].

Please cite this article as: G.B. Cerati, et al., Nucl. Instr. and Meth. A (2009), doi:10.1016/j.nima.2008.11.114

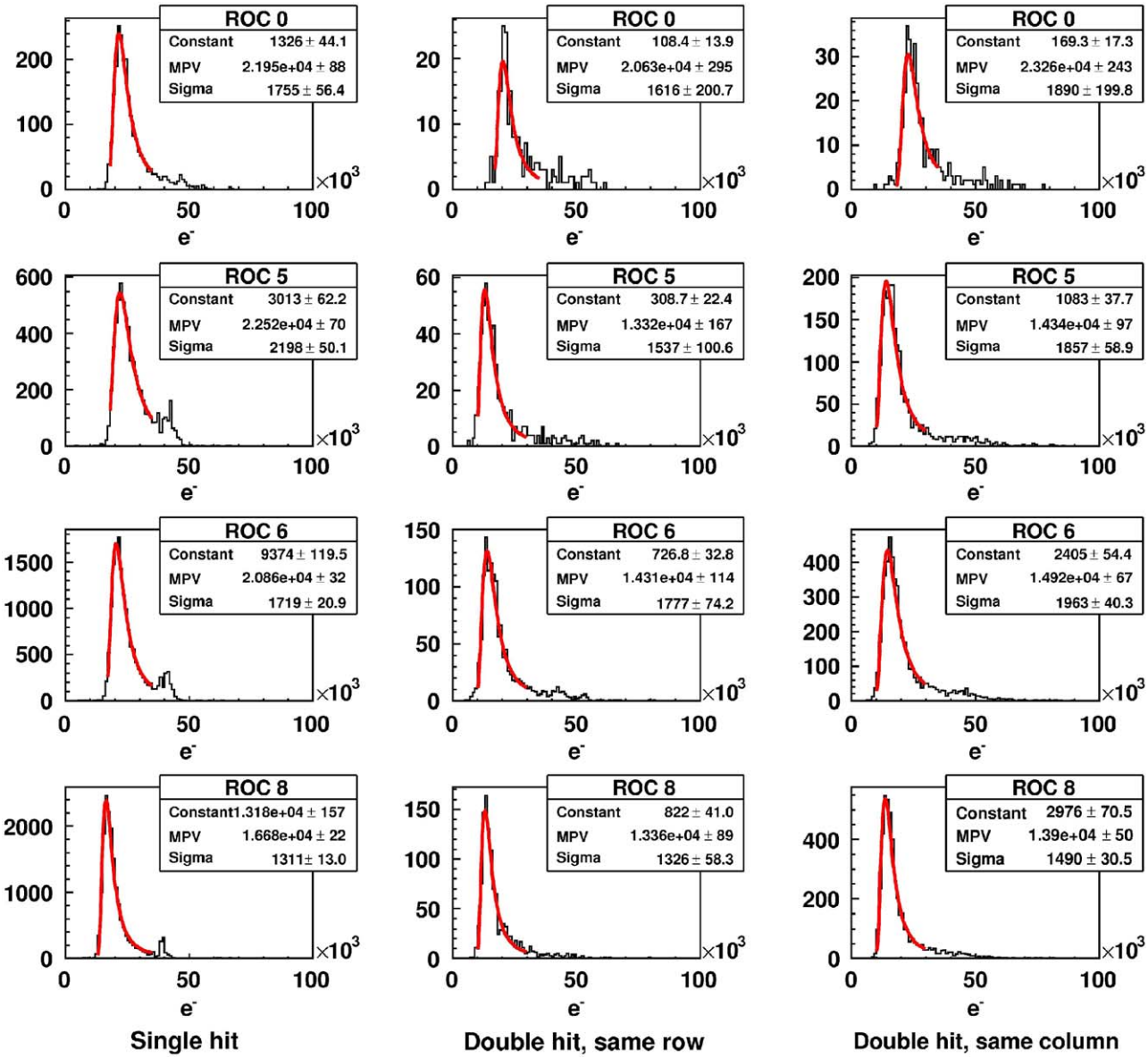

Fig. 6. On the left column, the single-hit spectra for particles fully contained in a single pixel; on the central column, the double-hit spectra for two adjacent pixels on the same row; on the right column, the double-hit spectra for two adjacent pixels on the same column. The spiky structure around 40 ke$^-$ in the single-hit spectra is due to the different gain-saturations of the pixel analog channels, which tend to cluster around that value.

boundaries by at least 20 μm in *X* and 30 μm in *Y*. The asymmetry in this selection cut is simply due to the different resolution provided by the telescope track along *X* and *Y*-coordinates. By way of contrast, whenever the track impact point is close to an edge by more than 20 μm in *X* or 30 μm in *Y*, but not simultaneously (to exclude the corner regions), the sum of the charges collected by the pointed pixel and the adjacent pixel is plotted in the central-column histograms, if the two adjacent pixels were on the same row, or in the right-column histograms, if they were on the same column. In either case, both of the involved pixels are required to have a signal above the threshold.

The resulting picture is that the region of sensor furthest away from the dose peak, ROC 5, can still collect all the released charge, provided it is not shared between adjacent pixels. As soon as we move toward the most irradiated region, the reduced carrier lifetime limits the charge-collection efficiency and lowers the Landau peak to about 93% of the expected value at ROC 6 and about 75% at ROC 8.[4] A further degradation of the signals is evident whenever more than one pixel is involved in the charge-collection process. In this case the amount of charge collected by two adjacent pixels on the same column is systematically larger than that collected by two pixels on the same row. This difference is due to the break on the p-stop ring in the region between any adjacent pixels on the same column. The interruption of the p-stop, indeed, increases locally the charge collection efficiency. There is also a clear indication that the percentage of lost charge with respect to that of the single hits diminishes moving toward

[4] Note that the sensor at ROC 8 might still not be fully depleted.

Please cite this article as: G.B. Cerati, et al., Nucl. Instr. and Meth. A (2009), doi:10.1016/j.nima.2008.11.114

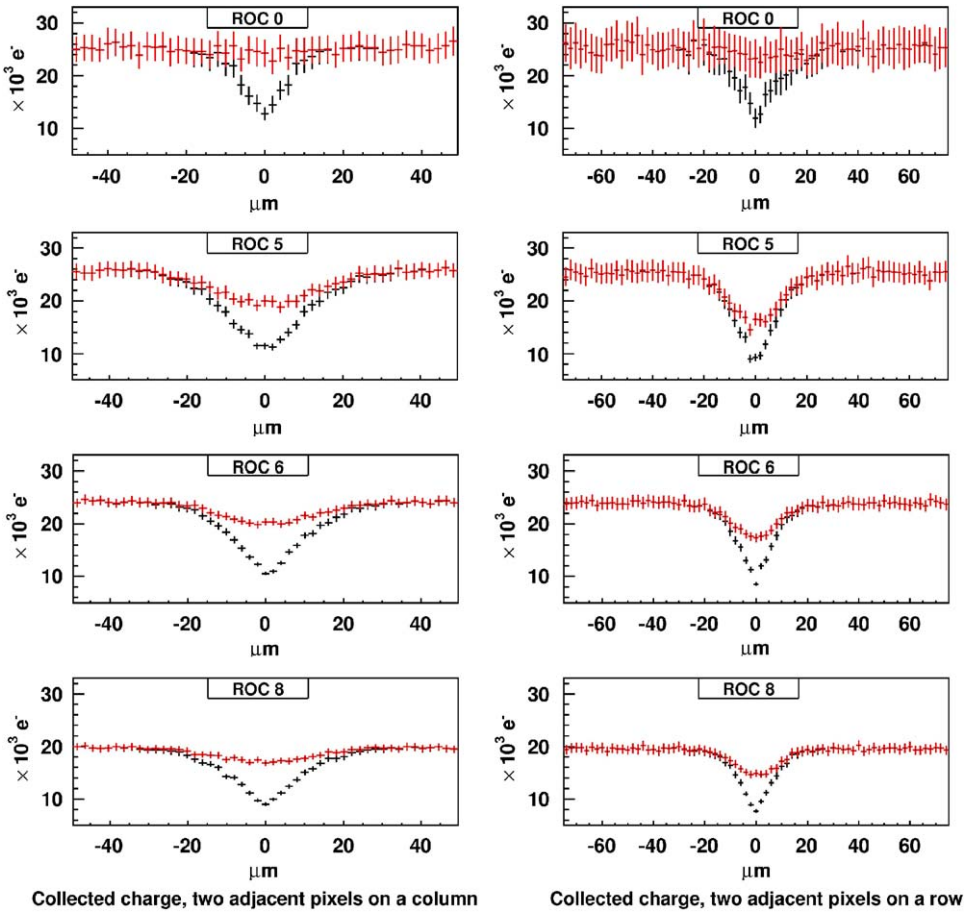

Fig. 7. The black points show the average collected charge by the sole pixel pointed by the track as a function of the distance of the track impact point from the boundary of the two adjacent pixels on the same column (histograms on the left) or on the same row (histograms on the right). The red points show the average sum of charges collected by the pixel pointed by the track and the adjacent one on the same column (histograms on the left) or on the same row (histograms on the right).

the most irradiated ROC 8. This means that, at high radiation doses, the charge collection efficiency in the region between pixels decreases with a much lower rate than near the center of the pixels. This could be attributed to the drastic changes of the electric-field expected at high radiation-doses. Indeed, the formation of a new junction on the *n*+ side, as a result of the type-inversion mechanism, radically changes the field configuration between adjacent pixel-implants.

The charge-collection features are further investigated in Fig. 7. Here, the average collected charge is plotted as a function of the signed distance of the track impact-point from the boundary of two adjacent pixels on the same column (Fig. 7, left column) and on the same row (Fig. 7, right column). To avoid additional sharing with other pixels, the track impact point is required to stay well within the column edges in the former case and the row edges for the latter. The usual fiducial cut of 20 μm in *X* or 30 μm in *Y* was applied. The two types of data points refer to the charge collected by the sole pixel pointed by the track (black points) and the sum of charges collected by the two adjacent pixels (red points).[5]

It turns out that the total amount of charge collected by ROC 0 shows a marginal deficit (a few percent) in crossing the region between two adjacent pixels, whereas the one collected by the irradiated detector shows a clear drop, reaching about 40% of the asymptotic (far from zero) value in the worst case. Also in this case, there is a clear evidence for an asymmetry in charge loss when comparing sharing between two pixels on the same column and on the same row.

In a completely analogous way, the measured detection efficiency is shown in Fig. 8 as a function of the signed distance of the track impact point from the boundary of the two adjacent pixels on the same column or the same row. The usual fiducial cuts were applied to exclude additional sharing with other pixels. Also here, the two types of data points refer to the sole efficiency of the pixel pointed by the track (black points) and the combined efficiency of the two adjacent pixels (red points). The combined efficiency is constant and does not show any appreciable degradation even in the region between pixels. The asymptotic efficiency, away from the pixel edge, reaches a value around 99%, fully consistent with 100%, given the ~1% systematic inefficiency of our apparatus.[6]

The complete two-dimensional point detection efficiency is shown in Fig. 9. Here, the efficiency of the single pixel pointed by

[5] A common saturation limit of 35 ke⁻ was imposed on both single-hit and double-hit signal charge to obtain consistent and directly comparable average-values.

[6] When two events are closer than 500 ns, the pixel hits of the second event, and only those coming from the CMS pixel under test, are lost by our data-acquisition system. This causes a systematic inefficiency of about 1% at the beam intensities we ran our tests.

Please cite this article as: G.B. Cerati, et al., Nucl. Instr. and Meth. A (2009), doi:10.1016/j.nima.2008.11.114

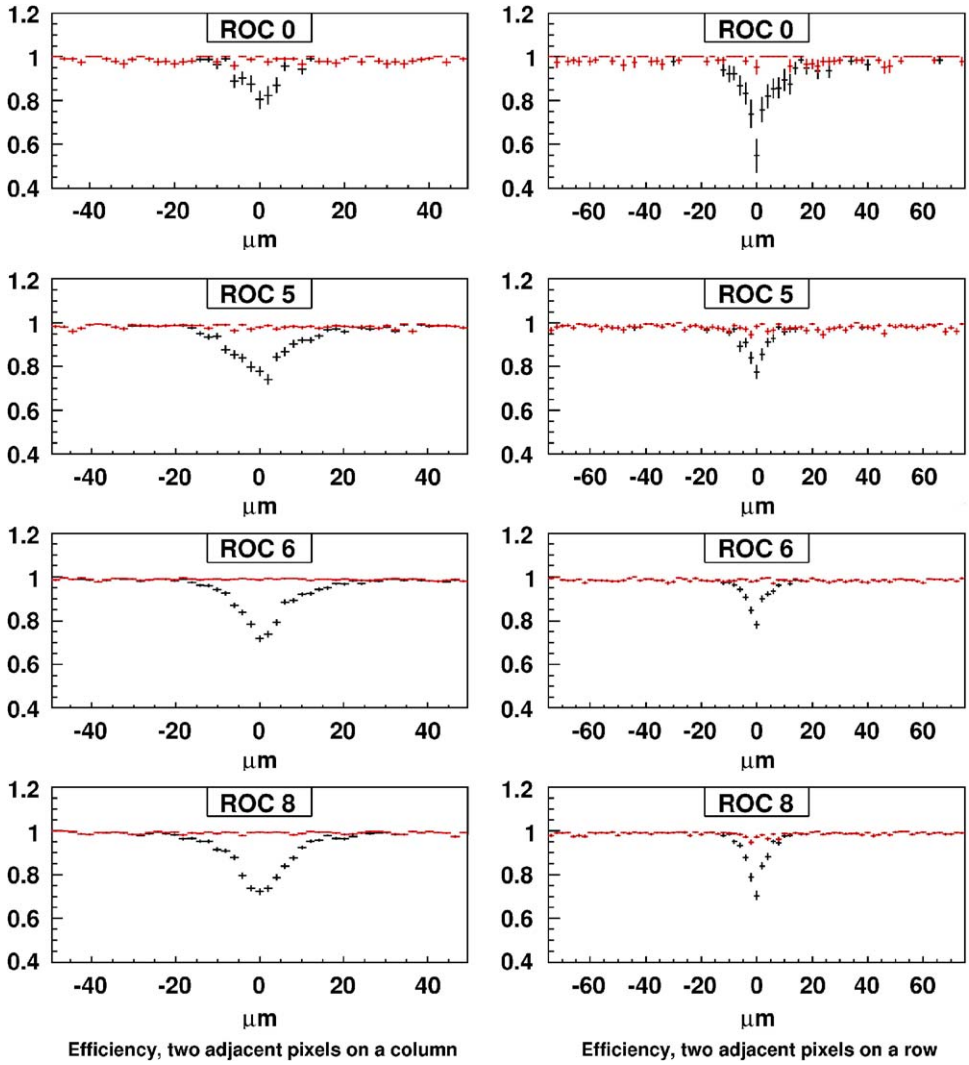

Fig. 8. The black points show the detection efficiency of the sole pixel pointed by the track as a function of the distance of the track impact point from the boundary of the two adjacent pixels on the same column (histograms on the left) or on the same row (histograms on the right). The red points show the combined efficiency of the pixel pointed by the track and the adjacent one on the same column (histograms on the left) or on the same row (histograms on the right).

the track is plotted together with the combined detection efficiency of the four nearby pixels. The inefficiency is confined near the corners of the pixels, where the fractions of signal collected by the single pixels are small and could easily fall below the threshold or outside the synchronization time-window because of time-walk. The resulting global detection efficiency is 98.61%±0.15% for ROC 0, 97.69%±0.10% for ROC 5, 98.78±0.05% for ROC 6 and 97.46±0.06% for ROC 8. It is worth noting that the maximum achievable efficiency would be in any case limited to ~99%, given the ~1% systematic detection inefficiency of our readout system.

The measured charge-sharing correlation between two adjacent pixels is plotted in Fig. 10 for cells belonging to the same column (plots on the left) and the same row (plots on the right). The two axes represent the amount of charge collected in each event by the two adjacent pixels respectively. Fiducial cuts were applied to exclude the corner regions as for Fig. 6. The well-behaved characteristic exhibited by the non-irradiated detector deteriorates as one moves toward the most irradiated region corresponding to ROC 8.

The position resolution achievable in case of charge-sharing between two adjacent pixels was investigated using the variable $\eta=Q_r/Q_l+Q_r$, where Q_l is the charge collected by the pixel on the left side and Q_r that on the right side of their interface. The distribution of measured η is shown in Fig. 11 for two pixels on the same row and on the same column of the four ROCs. The fiducial cuts used for these distributions are exactly the same as those for Fig. 7.

The peaks at 0 and 1 are due to events with one hit only on the left or right pixel respectively, i.e., no shared charge. The gap between the central portions of the distributions and the two peaks at 0 and 1, respectively, is caused by the threshold cut. In addition, the continuous effective increase of the threshold value, due to the loss of collected charge (as observed in Fig. 6), shrinks the central portion of the η-distribution when moving toward the most irradiated regions. The slight asymmetry with respect to the central η-value, present, at high radiation doses, in the distributions for adjacent pixels on the same row, cfr ROC 6 on the left, is due to the non-perfect orthogonality of the detector to the beam tracks. The plaquette was at an angle of about 60 mrad around X

Please cite this article as: G.B. Cerati, et al., Nucl. Instr. and Meth. A (2009), doi:10.1016/j.nima.2008.11.114

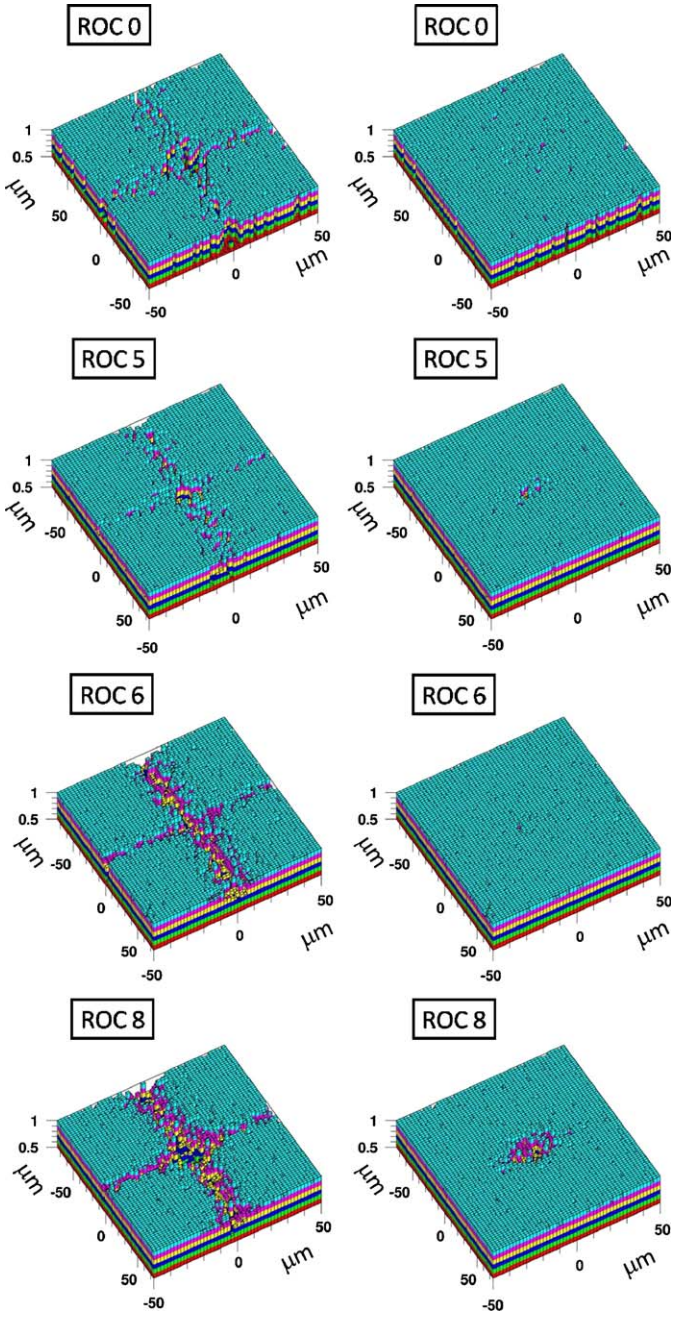

Fig. 9. The detection efficiency as a function of the coordinates of the track impact point. On the left plots the efficiency of the sole pixel pointed by the track, on the right ones the combined detection efficiency of the four nearby pixels.

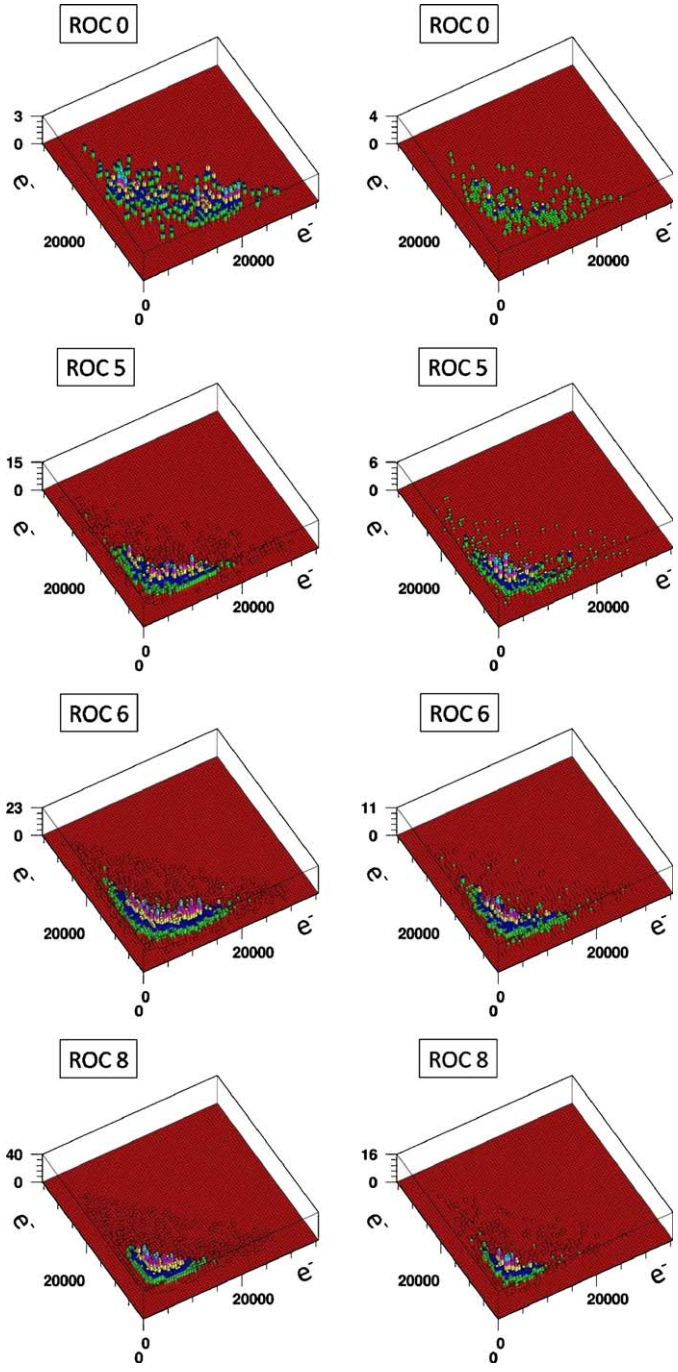

Fig. 10. The measured charge-sharing correlation between two adjacent pixels on the same column (plots on the left) or the same row (plots on the right).

and 50 mrad around Y from the orthogonal plane. These angles tilt the flat portion of the η-distributions when the charge-collection efficiency drops moving away from the pixel electrodes as for irradiated sensors. There is an evident excess of population on the right side of η-distributions for pixels belonging to the same column on ROC 6. Here, the effects of the non-orthogonality to the beam are superimposed with those due to the p-stop break, which further unbalances the charge-sharing in favor of the pixel on the right. To support this explanation, a study was conducted isolating the tracks impinging in the region corresponding to the p-stop breaks. It was found that the asymmetry of the resulting η-distribution becomes much larger and that, on the complementary area, tends to vanish. The same kind of asymmetry, though at a lower level, is also present on ROC 5. On ROC 8, the most irradiated one, the potentially huge excess disappears simply because it is cut out by the high effective value of the threshold. Also in this case, in a completely analogous way with what we found for the collected charge distributions above, we observe an effect which becomes stronger at higher absorbed doses and indicates a relative effective increase of the charge-collection efficiency in the region between adjacent pixels.

The correlation between the track impact point distance from the two-pixel interface and the measured η-value is shown in Fig. 12 with the usual meaning of the eight plots. Here, the

Please cite this article as: G.B. Cerati, et al., Nucl. Instr. and Meth. A (2009), doi:10.1016/j.nima.2008.11.114

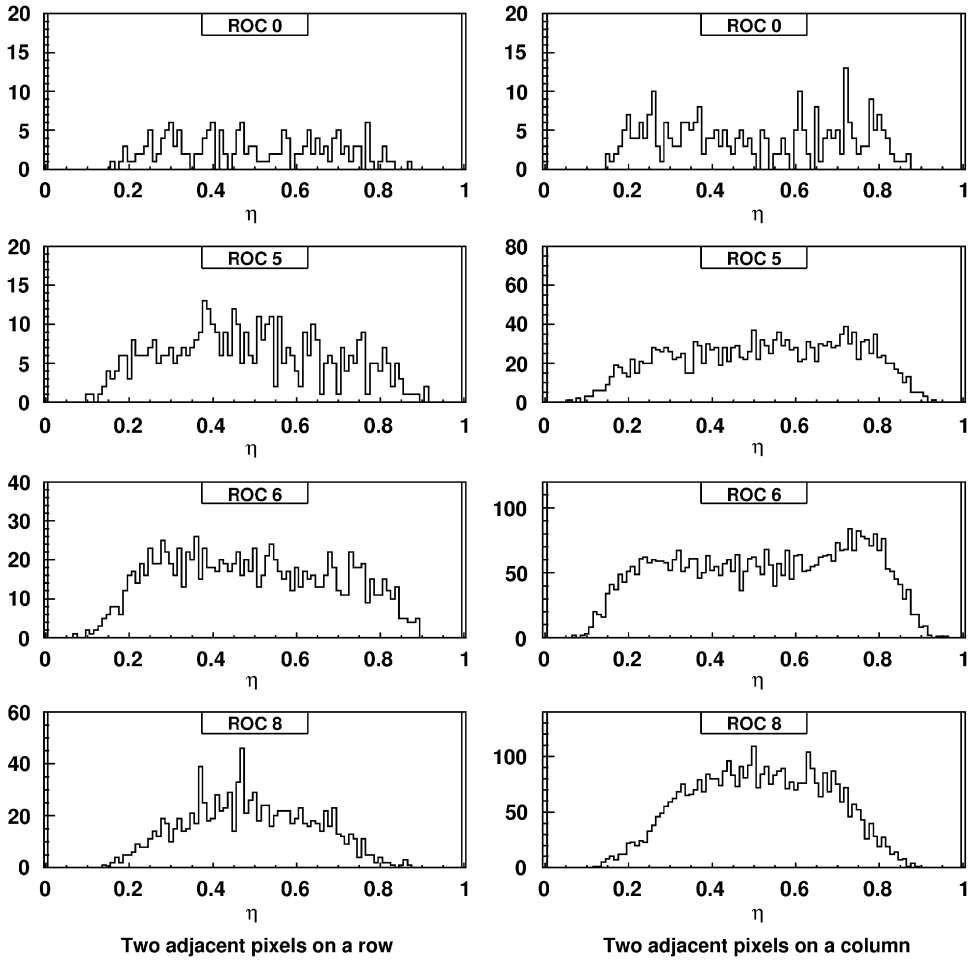

Fig. 11. The measured η-spectra for two adjacent pixels on the same row, histograms on the left, and on the same column, histograms on the right, of the four ROCs.

mean value of the signed distance of the track impact points within a certain η-bin was directly computed.

The same correlation was also investigated using an indirect method, which relies on the assumption that, on average, a higher η-value corresponds to a higher signed distance, x, from the pixel interface. In this case, one can easily demonstrate that the signed distance for a certain value of η, $x(\eta)$, is given by

$$\int_{-p}^{x(\eta)} \frac{dN_x}{dx}\, dx = \int_{0}^{\eta} \frac{dN_\eta}{d\eta}\, d\eta$$

where p stands for one half the pitch in x direction, dN_x/dx is the distribution of the signed distances, x, of the track impact point and $dN_\eta/d\eta$ that of the measured η. The resulting correlation plots are shown in Fig. 13. The two correlation plots obtained with the two methods substantially match each other.

The last measurement reported here is the observed hit-cluster size. This is shown in Table 1 as percentage of occurrence of a particular cluster size with respect to the total number of clusters.

It is hard to draw any quantitative conclusion from this table. Nevertheless, one can say that, because of the lower charge-collection efficiency induced by the radiation damage and, hence, an effective higher threshold value, the amount of sharing diminishes moving from ROC 5 to ROC 8. On ROC 8 the sharing is practically identical to that of the non-irradiated ROC 0, which, indeed, had a threshold (3800 e^-) higher than that of the other ROCs (3300 e^-).

4. Conclusions

The performance of the forward pixel detector of the CMS experiment was studied in a test-beam up to a maximum absorbed dose of 45 Mrad. The most evident sign of the radiation-induced damages at the highest dose was the reduction of ~25% of the signal released by a minimum ionizing particle. The detection efficiency, though, remains very high, ~99%, even at an equivalent threshold of about 3300 e^- and just shows some marginal drop near the pixel corners at the highest absorbed dose. There is an apparent relative increase of the charge-collection efficiency in the inter-pixel region at high radiation dose, which, in presence of the p-stop breaks, alters the symmetry of the η-distributions. In principle, this should be taken into account when interpolating the charge to extract the coordinate.

In conclusion, despite the observed damages, the detector remains fully operational and certainly suitable to accomplish the CMS physics goals at the expected fluence after several years of running at the LHC luminosity.

Please cite this article as: G.B. Cerati, et al., Nucl. Instr. and Meth. A (2009), doi:10.1016/j.nima.2008.11.114

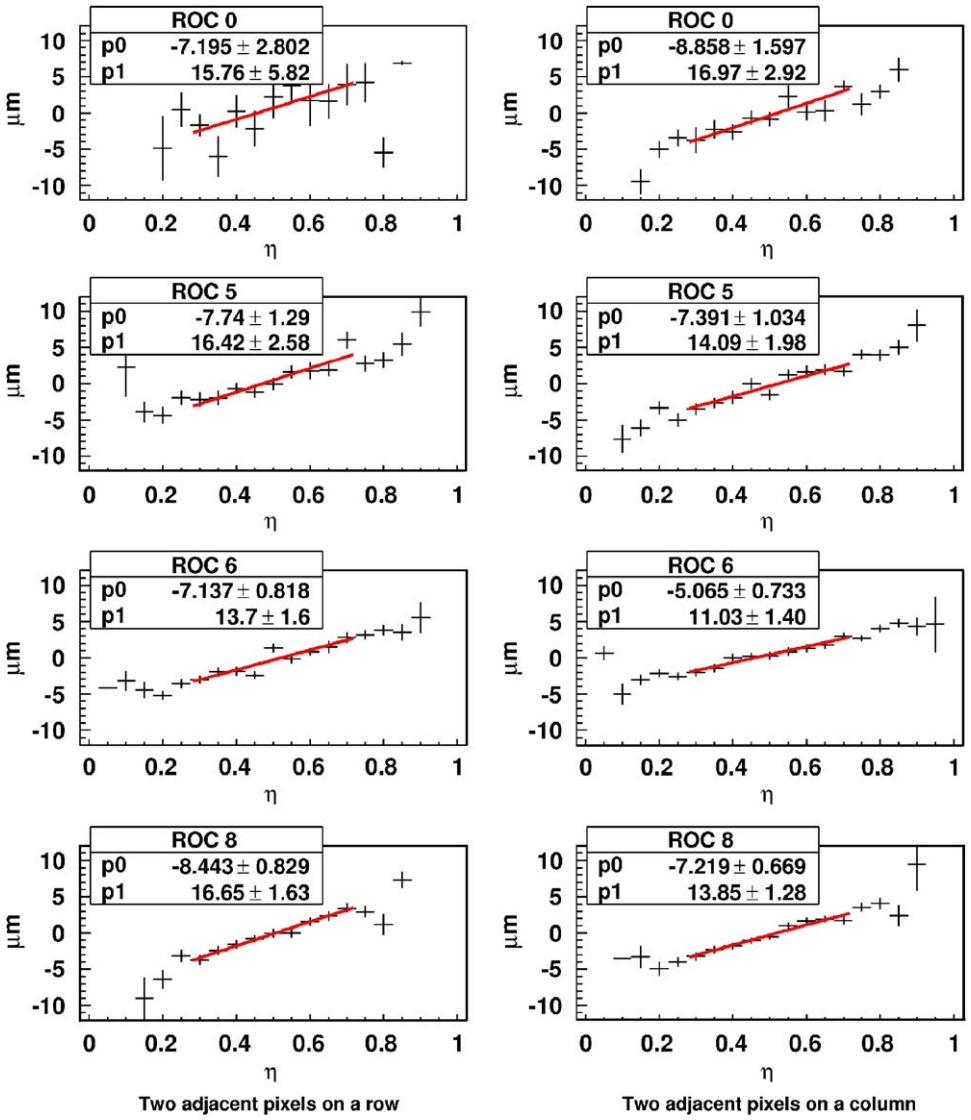

Fig. 12. The measured correlation between the track impact point distance from the two pixel interface and the measured η-value. The histograms on the left are for adjacent pixels on the same row, those on the right for adjacent pixels on the same column.

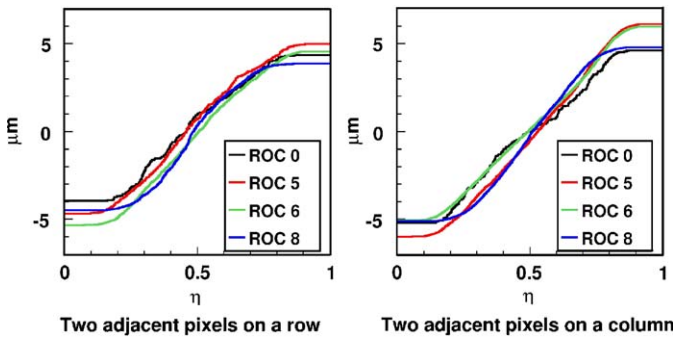

Fig. 13. The correlation between the track impact point distance from the two pixel interface and the measured η-value obtained by the indirect method described in the text. As for Fig. 12, the plots on the left are for adjacent pixels on the same row, whereas those on the right for adjacent pixels on the same column.

Table 1
The observed hit-cluster size for the four ROCs under test.

Cluster size	ROC 0 (%)	ROC 5 (%)	ROC 6 (%)	ROC 8 (%)
1	85.42 ± 0.70	81.78 ± 0.43	82.03 ± 0.28	85.57 ± 0.27
2	12.75 ± 0.66	16.00 ± 0.40	15.17 ± 0.26	12.73 ± 0.26
3	0.75 ± 0.17	1.15 ± 0.12	1.29 ± 0.08	0.84 ± 0.07
4	0.83 ± 0.18	0.72 ± 0.09	1.05 ± 0.07	0.55 ± 0.06
5	0.08 ± 0.06	0.12 ± 0.04	0.21 ± 0.03	0.14 ± 0.03
6	0.08 ± 0.06	0.10 ± 0.04	0.21 ± 0.03	0.06 ± 0.02

The percentage of occurrence of a certain cluster size is normalized to the total number of clusters.

Please cite this article as: G.B. Cerati, et al., Nucl. Instr. and Meth. A (2009), doi:10.1016/j.nima.2008.11.114

Acknowledgments

The authors would like to express gratitude to the colleagues from the Laboratory of Particle Physics at PSI and ETH-Zürich for sharing their knowledge of the PSI46V2 chip and the pixel detector in general. We would also thank colleagues from Purdue University and Gino Bolla in particular for their fruitful collaboration to interpret these results. Finally, we wish to acknowledge the assistance of the staffs of Fermi National Accelerator Laboratory, the Italian Istituto Nazionale di Fisica Nucleare and the physics departments of the collaborating institutions.

References

[1] R. Adolfi, et al., The CMS experiment at the CERN-LHC, JINST 3: S08004, 2008.
[2] H.C. Kästli, Nucl. Instr. and Meth. A 565 (2006) 188.
[3] P. Bhat, N. Mokhov, A. Singh, Beam radiation simulation in CMS, CMS Internal Report, 12 December, 2007.
[4] L. Uplegger, et al., IEEE Trans. Nucl. Sci. NS-53 (2006) 409.
[5] D. Menasce, M. Turqueti, L. Uplegger, Nucl. Instr. and Meth. A 579 (2007) 1141.
[6] ftp://root.cern.ch/root/doc/5FittingHistograms.pdf.

Please cite this article as: G.B. Cerati, et al., Nucl. Instr. and Meth. A (2009), doi:10.1016/j.nima.2008.11.114